



HAL
open science

Investigating the lateral resolution of the surface wave focal spot imaging technique using two-dimensional acoustic simulations

Bruno Giammarinaro, Christina Tsarsitalidou, Gregor Hillers

► **To cite this version:**

Bruno Giammarinaro, Christina Tsarsitalidou, Gregor Hillers. Investigating the lateral resolution of the surface wave focal spot imaging technique using two-dimensional acoustic simulations. 2022. hal-04155285v1

HAL Id: hal-04155285

<https://hal.science/hal-04155285v1>

Preprint submitted on 7 Jul 2023 (v1), last revised 29 Feb 2024 (v2)

HAL is a multi-disciplinary open access archive for the deposit and dissemination of scientific research documents, whether they are published or not. The documents may come from teaching and research institutions in France or abroad, or from public or private research centers.

L'archive ouverte pluridisciplinaire **HAL**, est destinée au dépôt et à la diffusion de documents scientifiques de niveau recherche, publiés ou non, émanant des établissements d'enseignement et de recherche français ou étrangers, des laboratoires publics ou privés.



Distributed under a Creative Commons Attribution 4.0 International License



Investigating the lateral resolution of the surface wave focal spot imaging technique using two-dimensional acoustic simulations

Bruno Giammarinaro^{® a}, Christina Tsarsitalidou^{® a} and Gregor Hillers^{® a}

^a Institute of Seismology, University of Helsinki, 00014 Helsinki, Finland

E-mails: email: bruno.giammarinaro@helsinki.fi (B. Giammarinaro), email: christina.tsarsitalidou@helsinki.fi (C. Tsarsitalidou), email: gregor.hillers@helsinki.fi (G. Hillers)

Abstract. We investigate the lateral resolution power of the seismic Rayleigh wave focal spot imaging technique. We use two-dimensional acoustics simulations in a closed cavity for the passive Green's function and focal spot reconstruction. Four different velocity distribution configurations target different resolution aspects. The finite data range that is necessary to constrain the Bessel function model controls the lateral spreading of material contrasts, the distinction of two objects on sub-wavelength scales, and the image quality of complex random media. Good data quality from dense networks supports short range estimates and super-resolution.

Keywords. Numerical modeling, wave propagation, seismic noise, cavity, focal spot, resolution, seismic imaging.

This article is a draft (not yet accepted!)

1. Introduction

Disadvantages of earthquake tomography associated with limited illumination can now be compensated by ambient noise tomography with its flexible virtual source and receiver configurations. Both approaches invert far-field observations of travel time differences, obtained from earthquake seismograms or from passive Green's function reconstructions, for an optimal model of the velocity structure [Tromp et al., 2005, Liu and Gu, 2012, Shapiro and Campillo, 2004, Sabra et al., 2005].

Modern dense seismic arrays support alternative local surface wave speed estimations from noise correlation functions [Lin et al., 2009, Lin and Ritzwoller, 2011], which includes the large scale application of the frequency domain spatial autocorrelation (SPAC) method [Aki, 1957, Ekström et al., 2009, Ekström, 2014] that is otherwise typically applied to local sparse array data [Asten, 2006]. Such dense arrays can now contain on the order of 1000 sensors, which facilitates the proper sampling of the noise correlation amplitude distribution in the near-field. At zero lag time, the time domain representation of the spatial autocorrelation field is referred to as focal spot, which contains the same information as SPAC and can be analyzed using the same mathematical tools [Cox, 1973, Yokoi and Margaryan, 2008, Tsai and Moschetti, 2010, Haney et al., 2012, Haney and Nakahara, 2014].

Near-field or focal spot analysis is used in applications that work with a high sensor density. Focal spots have first been studied in time-reversal experiments in underwater acoustics and medical imaging [Fink, 1997]. Initially, noise correlation medical imaging transferred the noise seismology approaches to passive elastography, first using far-field surface waves along muscle fibers [Sabra et al., 2007], later using refocusing shear waves. Different properties of the shear wave focal spot have been analyzed including its one-dimensional width [Catheline et al., 2008, Gallot et al., 2011], two-dimensional shape [Benech et al., 2013, Brum et al., 2015], and its curvature [Catheline et al., 2013], which can all be reconstructed using MRI [Zorgani et al., 2015] and ultrasound [Barrere et al., 2020] speckle tracking methods. Importantly, Zenzemi et al. [2020] demonstrated that the ability to discriminate two objects is not controlled and hence limited by the shear wavelength, but instead by the ultrasonic frequency and the pixel density. In seismology, this corresponds to the array station density.

Hillers et al. [2016] first applied Rayleigh wave focal spot imaging in seismology to image lateral velocity variations in a fault zone environment. As for SPAC, the phase velocity is estimated from the focal spot shape using Bessel function models. Using numerical time-reversal experiments based on a Green's function calculator [Cotton and Coutant, 1997] for one-dimensional layered media, Giammarinaro et al. [2023] demonstrated the feasibility to accurately estimate phase velocity and dispersion using noisy reconstructions, for non-isotropic surface wave illumination, and in the presence of P -waves using a fitting range around one wavelength. Whereas the results from Giammarinaro et al. [2023] suggest the overall robustness and utility of the focal spot method for seismic imaging applications, most notably because of the increase in depth resolution, the study could not address lateral resolution. Considering that super-resolution can be obtained with tip-curvature measurements [Zenzemi et al., 2020], it is important to assess the effect of the fitting range on speed estimates from densely sampled seismic focal spots.

Here we study systematically the lateral focal spot resolution using numerical experiments. We perform two-dimensional acoustics simulations to reconstruct the Green's function from reverberating wave fields (Section 2). The ambient field generated in a chaotic closed cavity [Draeger and Fink, 1999] yields results that are equivalent to results from open media noise correlation [Derode et al., 2003]. The obtained Green's function is identical and is here therefore taken as a proxy for seismic vertical-vertical component Rayleigh wave correlations [Sanchez-Sesma, 2006, Haney et al., 2012]. We work with a constant number of grid points and a fixed reference frequency. We implement four test cases and vary the data range or fitting distance r_{fit} to investigate the effect on the resolution of the velocity structure. These cases include a homogeneous control experiment (Section 3.1), an interface between two half-spaces (Section 3.2), circular inclusions (Section 3.3), and heterogeneous or random velocity distributions (Section 3.4). In Section 4 we discuss the different resolution aspects that are investigated with the variable configurations for a comprehensive evaluation of the seismic Rayleigh wave focal spot imaging performance.

2. Method

2.1. Synthetic experiments

This study is based on synthetic diffuse wave fields generated in a closed cavity. The resulting correlation functions are equivalent to noise correlations in open media [Derode et al., 2003]. Simulations are performed using the function `kSpaceFirstOrder2D` from the MATLAB toolbox `kWave` [Treeby et al., 2018]. This function solves a system of first-order acoustic equations for the conservation of mass and momentum using a wavenumber k -space pseudospectral method. The two-dimensional medium is composed of 500×500 grid points that are spaced in the x and y direction by $dx = dy = 0.1$ km (Fig. 1a). The background wave speed in the cavity is $V_0 = 2$ km/s. The closed cavity is implemented using different densities outside ($\rho_{\text{out}} = 59$ kg/m³) and inside ($\rho_{\text{in}} = 2950$ kg/m³) the cavity. Choosing ρ_{out} to be 2% of ρ_{in} creates strongly reflecting boundaries from impedance contrast without mitigating potentially problematic stability conditions associated with a large change in wave speed. We cannot exclude the occurrence of weak numerical dispersion in some of the heterogeneous case studies, but the overall consistency of the synthesized Green's functions and focal spots in the

different experiments suggests that this effect does not govern our results. Inside the cavity we select a square target domain consisting of 151×151 grid points where we record the solution. In this region we define the different velocity distributions introduced in section 2.2. Results for each of the four cases discussed in section 3 are obtained by averaging 11 independent wave field simulations. Each simulation starts with a point source at a different position inside the cavity (Fig. 1a). The source emits a 1 s long pulse centered at 1 Hz (Fig. 1b-c). The wave field is recorded for 300 s inside the square sub-domain with a 100 Hz sampling frequency.

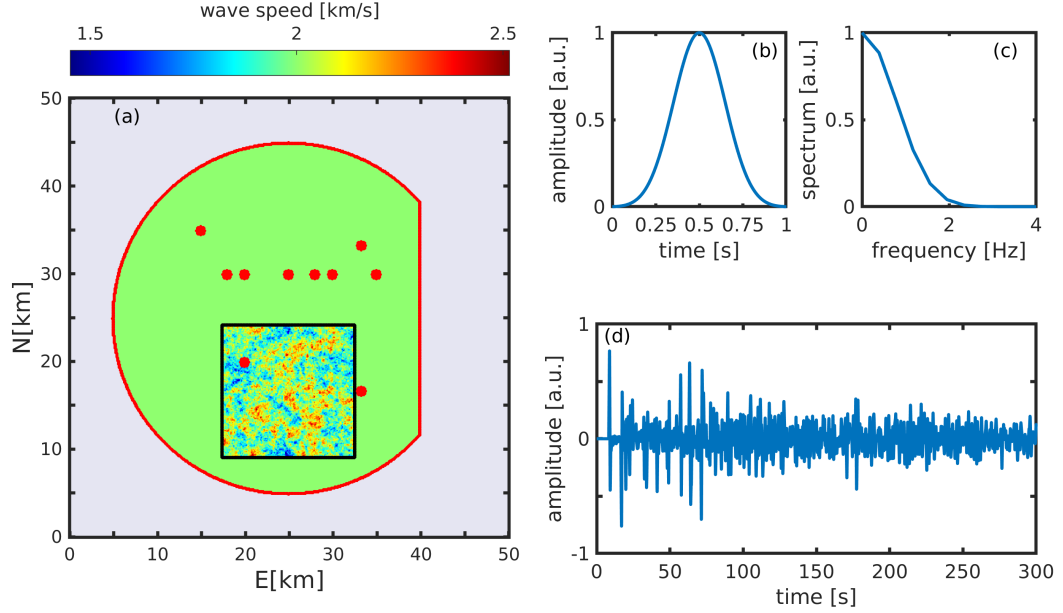


Figure 1. Configuration of the numerical experiments. (a) Representation of the closed cavity, with a background velocity $V_0 = 2$ km/s. The gray area represents the outer part of the medium with the same velocity but with an impedance contrast to trap the waves in the cavity. The red line is boundary of the closed cavity. The black line is boundary of the target area where the results are recorded. Inside the cavity the color corresponds to the input wave speed. Red dots indicate the source positions for the 11 realizations. Times series (b) and normalized power spectrum (c) of the emitted pulse used for each realization of the simulation. (d) Example of a full time-series recorded in the cavity.

2.2. The acoustic medium in the target domain

The acoustic wave speed distribution $V(\mathbf{x})$ is defined as a spatial function in the square target domain

$$V(\mathbf{x}) = V_0(1 + \xi(\mathbf{x})), \quad (1)$$

where $V_0 = 2$ km/s is the background wave speed in the cavity, \mathbf{x} is the position, and ξ is the relative change in wave speed, i.e., the parameter that controls the medium heterogeneity. In the following sections, the 2 km background wavelength at 1 Hz is denoted λ_0 . In section 3 we begin with a control experiment of a homogeneous medium with $\xi = 0$ to study the overall system response.

2.3. Lateral spreading across two welded half-spaces

We modify the homogeneous control experiment and replace the 2 km/s velocity in left half of the target domain by an increased 2.2 km/s value. In our 2D configuration, this creates two half-spaces which allows us to investigate the lateral resolution as the imaging method induced spreading or widening of the sharp interface. Such sharp lateral velocity contrasts can occur across bimaterial interfaces in fault zone environments [Weertman, 1980, Ben-Zion, 1989], or in the contact region of intrusions with the host rock [Chamarczuk et al., 2019].

2.4. Resolution of circular inclusions

Next we perform a classic resolution test and study the power of the method to separate two individual entities in an image. For this we impose three pairs of circular inclusions separated by $0.25\lambda_0$, $0.5\lambda_0$ and $1\lambda_0$. The inclusions have a diameter of $1\lambda_0$. We test two different sets, where one set of inclusions is stiffer than the background with $\xi = 25\%$, and the other set has more compliant inclusions compared to the background with $\xi = -25\%$. Such a ‘two-body problem’ is typically studied in gel phantom experiments performed in medical ultrasound imaging or medical imaging for tumor detection [Catheline et al., 2013, Zemzemi et al., 2020]. It is a less common configuration in seismology where so-called checkerboard tests are commonly employed to quantify the resolution of a tomographic configuration. Circular cross section features can occur in the context of magmatic intrusions or conduits. However, as said, with this configuration we can study the lateral resolution defined as the minimum distance between objects that the method allows to discriminate in an image. This study is performed with different fitting ranges r_{fit} discussed in section 2.6.

2.5. Randomly distributed wave speeds

Last we consider random media using a functional form that is often used to parameterize the distributions of variables such as wave speed, stress, or frictional properties in Earth materials [Frankel and Clayton, 1986, Holliger and Levander, 1992, Mai and Beroza, 2002, Ripperger et al., 2007, Sato et al., 2012, Obermann et al., 2016, Hillers et al., 2007]. We define $\xi(\mathbf{x})$ through a spatial 2D inverse Fourier transform as

$$\xi(\mathbf{x}) = \text{FT}^{-1} \left[\sqrt{P(\mathbf{k})} e^{i\phi(\mathbf{k})} \right], \quad (2)$$

where \mathbf{k} is the spatial wavenumber of the 2D distribution, $P(\mathbf{k})$ is the power spectral density, and $\phi(\mathbf{k})$ is a random distribution of the phase between 0 and 2π . The random distribution is calculated using the Python *randn* function coupled with a seed fixed to 3. Fixing the seed allows to randomly generate the phase and to keep the same distribution to observe the effect of the control parameters. The power spectral density $P(\mathbf{k})$ follows the von Karman probability function [Sato et al., 2012]

$$P(\mathbf{k}) = \frac{4\pi\Gamma[\kappa + 1]\epsilon^2 a^2}{\Gamma[\kappa](1 + a^2\|\mathbf{k}\|^2)^{\kappa+1}}. \quad (3)$$

The correlation length of the modeled parameter is a , ϵ governs the contrast in the medium, κ defines the sharpness of the spectral decay, and Γ is the Gamma function. We use equation 3 to generate nine different media with variable a and κ (Table 1), and constant $\epsilon = 150 \text{ km}^{-1}$.

2.6. Data processing and wave speed estimation

Data processing is performed in a Python3.8 environment. For each simulation, we analyze simulated data between 100 s and 300 s (Fig. 1d) to enhance the diffusive parts of the wave field (Fig. 2a). We filter the traces with a Gaussian filter centered at 1 Hz and with a width of 3.2%. We compute the normalized cross-correlation between each sensor pair to extract the spatial auto-correlation fields at zero lag time. Results are stacked over the 11 realizations for each case. This yields at short distances around a reference station the large-amplitude

Medium	1	2	3	4	5	6	7	8	9
a [km]	1	1	1	2	2	2	3	3	3
κ	0.1	0.3	0.6	0.1	0.3	0.6	0.1	0.3	0.6

Table 1. Parameters for the generation of different heterogeneous media using Equation 3, where a is the correlation length and κ governs the sharpness of the spectral decay. The corresponding wave speed distributions are displayed in Figure 8.

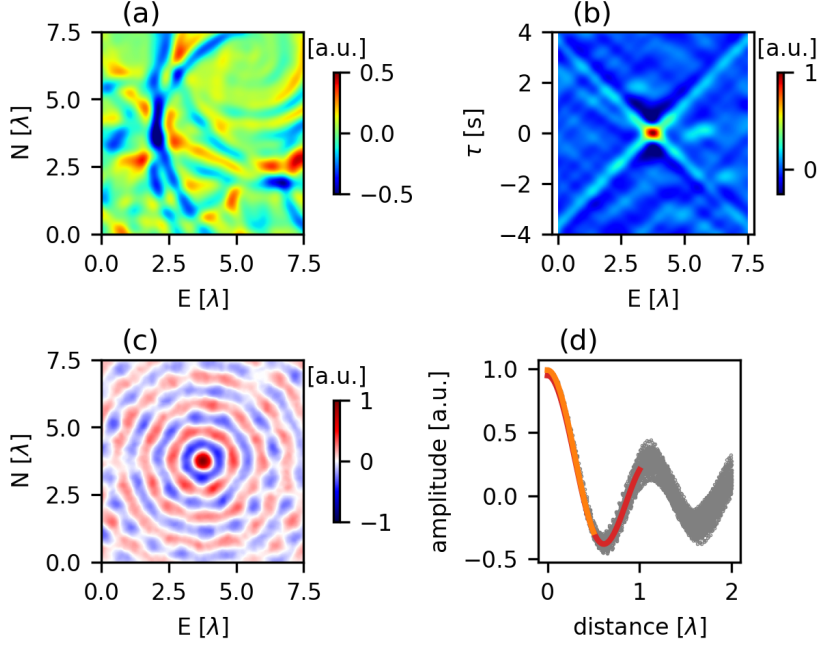


Figure 2. Workflow stage examples for the homogeneous medium. (a) Snapshot of a diffuse wave field. (b) Time-reversed space-time wave field obtained by cross-correlation. (c) Spatial auto-correlation with focal spot at the center obtained at 1 Hz after stacking over 11 realizations. (d) Simulated 1 Hz focal spot data (gray) and nonlinear regression results for $r_{\text{fit}} = 0.5\lambda_0$ (orange) and $r_{\text{fit}} = 1\lambda_0$ (red). In this and all subsequent figures the unit λ equals the 1 Hz wavelength λ_0 for the reference $V_0 = 2$ km/s.

feature referred to as focal spot (Fig. 2c). The shape is linked to the wave speed through the imaginary part of the Green's function. From each focal spot we estimate the wave speed $V = \omega/k$ free parameter by fitting the azimuthal averaged data to the $J_0(kr)$ model using a nonlinear least squares regression algorithm [Hillers et al., 2016, Giammarinaro et al., 2023, Giammarinaro and Hillers, 2022]. Again, the 2D acoustic configuration yields results that are identical to the lateral propagation of Rayleigh surface waves. The $J_0(kr)$ model equally describes the vertical-vertical component of the Rayleigh wave focal spot [Haney et al., 2012, Haney and Nakahara, 2014], and V is thus equivalent to the Rayleigh wave phase velocity c_R .

This process is performed for the 22801 focal spots, and each obtained V estimate is associated with the location of the reference station. This instantaneous imaging concept thus compiles velocity distributions across dense arrays without solving an inverse problem. Importantly, we choose two different fitting ranges r_{fit} of 1 km and 2 km associated with $0.5\lambda_0$ and $1\lambda_0$ at 1 Hz (Fig. 2d). Away from edges, this corresponds to 80 and 314 data-points. We vary r_{fit} because it is a critical tuning parameter, and values around one wavelength yield

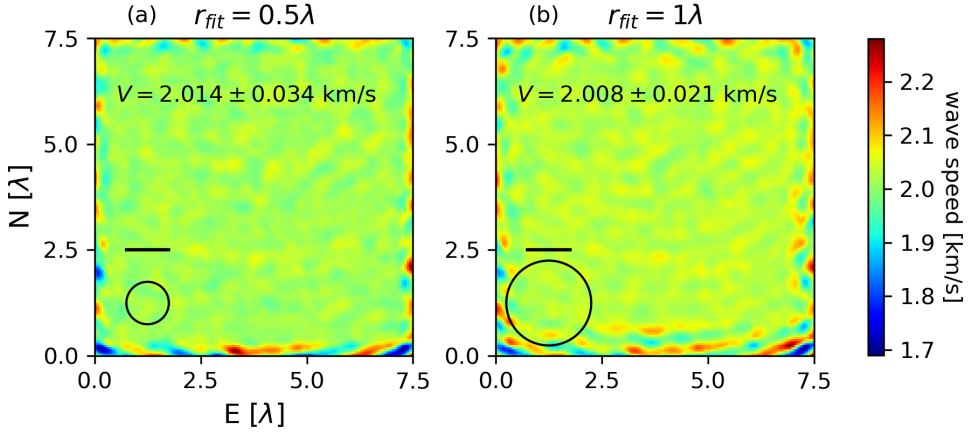


Figure 3. The control experiment. Focal spot obtained images for (a) $r_{\text{fit}} = 0.5\lambda_0$ and (b) $r_{\text{fit}} = 1\lambda_0$ for a homogeneous medium with wave speed $V = 2$ km/s. The reference wavelength λ_0 is indicated by the black line and the r_{fit} range used for the nonlinear regression is the radius of the black circle.

overall stable results [Giammarinaro et al., 2023]. Larger values can stabilize a regression for noisy signals, but the near-field focal spot imaging concept essentially invites the minimization of r_{fit} for improved resolution. This refers to improved depth resolution as c_R values can be estimated at wavelengths that cannot be studied with tomography [Tsarsitalidou et al., 2021, Giammarinaro et al., 2023], but also to the lateral resolution investigated here.

3. Results

3.1. The homogeneous reference case

The first test is the homogeneous control experiment which we use first to illustrate basic features of the approach. The simulations yield diffuse wave fields that can be used for focal spot imaging. Figure 2(a) shows a snapshot of a diffuse wave field, Figure 2(b) a time-space representation of the time-reversed correlation wave field, Figure 2(c) shows a focal spot of one realization, and Figure 2(d) shows the results of the nonlinear regression following the data processing described in section 2.6. In Figure 2(b) we can see the refocusing and diverging waves of the Green's function after cross-correlating the diffuse fields. However, the reconstruction is not perfect which is indicated by small-amplitude fluctuations. The time domain auto-correlation field shows the focal spot at small distances around the origin (Fig. 2c). The irregularity of the white zero-crossing contours again illustrates fluctuations and imperfect reconstruction after stacking over 11 realizations. We attribute this to non-perfectly diffuse wave fields associated with the modes in the cavity. Figure 2(d) displays results from the nonlinear regression using the two fitting distances $r_{\text{fit}} = 0.5\lambda_0$ and $r_{\text{fit}} = 1\lambda_0$. The spread in the data with increasing distance are the fluctuations from Figure 2(c).

The 2D V distributions obtained with $r_{\text{fit}} = 0.5\lambda_0$ and $r_{\text{fit}} = 1\lambda_0$ are displayed in Figure 3. The key feature in these images are the speckle patterns. They illustrate that the imperfect reconstruction propagates through the

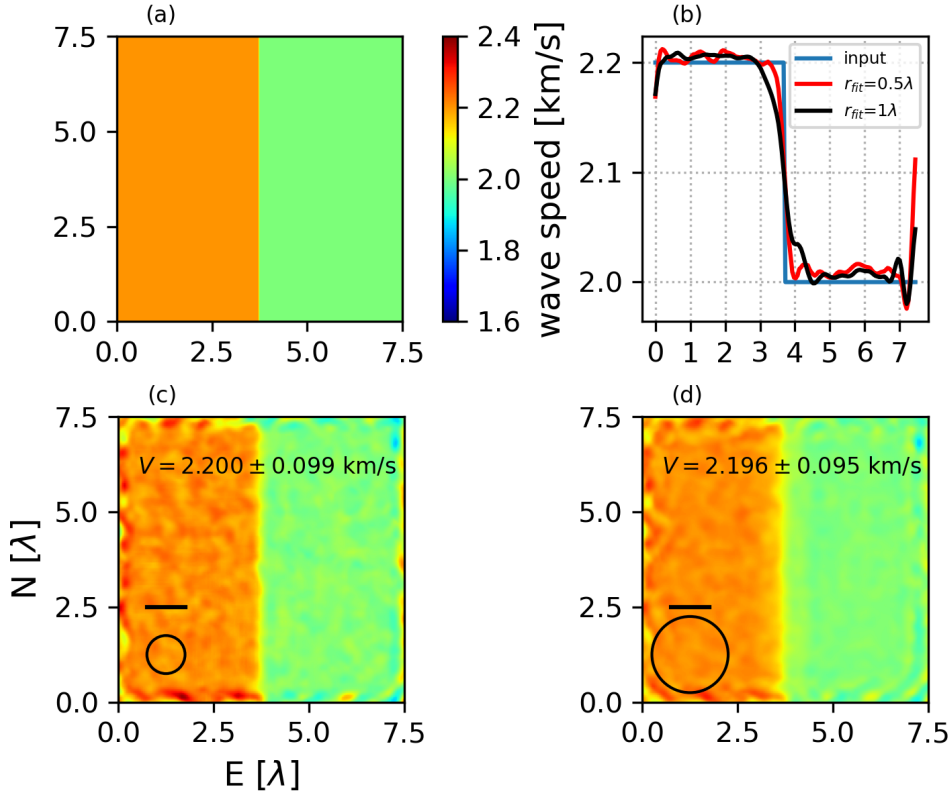


Figure 4. Results for the two half-spaces. (a) The input model. (b) Reference (blue) and focal spot based velocity profiles obtained with two fitting ranges (red, black) that are averaged along the N-axis. (c-d) Focal spot based images of the medium velocity. The reference wavelength λ_0 is indicated by the black line and the r_{fit} range used for the nonlinear regression is the diameter of the black circle.

measurement process to produce these fluctuations around the average reference value. Using $r_{\text{fit}} = 0.5\lambda_0$ and $r_{\text{fit}} = 1\lambda_0$ leads to $V = 2.014 \pm 0.034 \text{ km/s}$ and $V = 2.008 \pm 0.021 \text{ km/s}$, so the reference value is well recovered within an uncertainty level of 1.5% and 1%. Increasing the fitting range improves the estimation which tends to converge to $V_0 = 2 \text{ km/s}$. Another strong feature are the boundary effects. Recall that we only use values inside the square target area. The estimation error increases towards the borders and the affected regions appears to depend on the r_{fit} length. Evidently, the error is not equal along all boundaries but is largest along the southern edge. This is likely explained by the centered, low position of the target area in the cavity, together with the excitation of specific modes in the cavity that sustain a non-isotropic energy flux in the scattered wave field. These effects emerge in all other cases, they could potentially be mitigated by a different configuration or geometry, or by averaging over more sources located at more diverse locations, but these side effects do not affect our conclusions.

3.2. Resolution of the interface between half-spaces

Figure 4 displays the input wave speed distribution (Fig. 4a) and the focal spot-based images of two homogeneous half-space media for the fitting ranges $r_{\text{fit}} = 0.5\lambda_0$ (Fig. 4c) and $r_{\text{fit}} = 1\lambda_0$ (Fig. 4d). As for the control experiment, the distributions show small residual fluctuations around the accurately resolved input values,

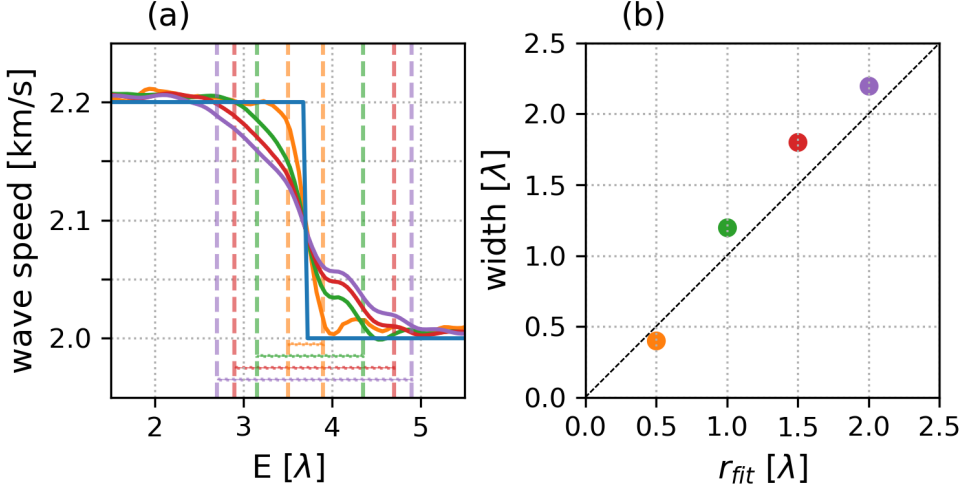


Figure 5. The dependence of the transition width on the data range. (a) Averaged wave speed profiles along the E-axis for the input (blue) and four different fitting ranges. The vertical dashed lines indicate the location where the amplitudes of the empirical profiles equal the 5% and 95% values of the 0.2 km/s velocity jump. The dotted lines indicate the estimates of the transition width ΔL . (b) The transition width ΔL as a function of fitting distance. Colors in (a) and (b) correspond to the same r_{fit} values.

and larger edge effects along the lower boundary. The obtained average wave speed of the stiffer medium is displayed on the panels, they can be considered equal within the error margins.

More interesting are the profiles across the domain shown in Figure 4(b). These profiles are averages along the N-axis. It is clear that the imaged distributions across the interface does not follow the blue input step function, but are instead spread out. To quantify the resolution we estimate the width ΔL of the transition. This is measured as the distance between the points where the amplitude of the empirical profile equals the 5% and 95% values of the 0.2 km/s velocity jump, i.e., when the values are 2.01 km/s and 2.19 km/s. Figure 5(a) enlarges the area around the interface located at $3.75\lambda_0$. It shows four profiles obtained with r_{fit} ranging from $0.5\lambda_0$ to $2\lambda_0$ in $0.5\lambda_0$ intervals. It confirms the previous observation that the overall velocity in each half-space is correctly estimated for every fitting ranges. As for the results in Figure 3 and Figure 4 we can perhaps discern a weak tendency to slightly overestimate the reference values. The width ΔL is shown in Figure 5(a) as dotted lines at the bottom, with the vertical dashed lines being the 5% and 95% boundaries of the transition zone. The calculated widths are compiled in Figure 5(b). For $r_{\text{fit}} = 0.5\lambda_0$, the transition zone has a width of $\Delta L = 0.4\lambda_0$. For $r_{\text{fit}} = 1\lambda_0$ we obtain $\Delta L = 1.2\lambda_0$, and for $r_{\text{fit}} = 2\lambda_0$, it is $\Delta L = 2.2\lambda_0$. The spreading effect quantified as the transition width between the two media can hence well be approximated to scale with the fitting range, $\Delta L \approx r_{\text{fit}}$.

3.3. Resolution and contrast of circular inclusions

We now examine the resolution of pairs of $1\lambda_0$ -wide circular inclusions separated by variable distances. The velocity in the inclusions increases and decreases by 0.5 km/s with respect to the background reference $V = 2$ km/s. Nonlinear regression of the focal spot data are also performed using fitting ranges $r_{\text{fit}} = 0.5\lambda_0$ and $r_{\text{fit}} = 1\lambda_0$. Figure 6 collects in the left two columns the input wave speed distributions, and the focal spot obtained images for $r_{\text{fit}} = 0.5\lambda_0$ and $r_{\text{fit}} = 1\lambda_0$. As a general observation, every inclusion is visible on the images

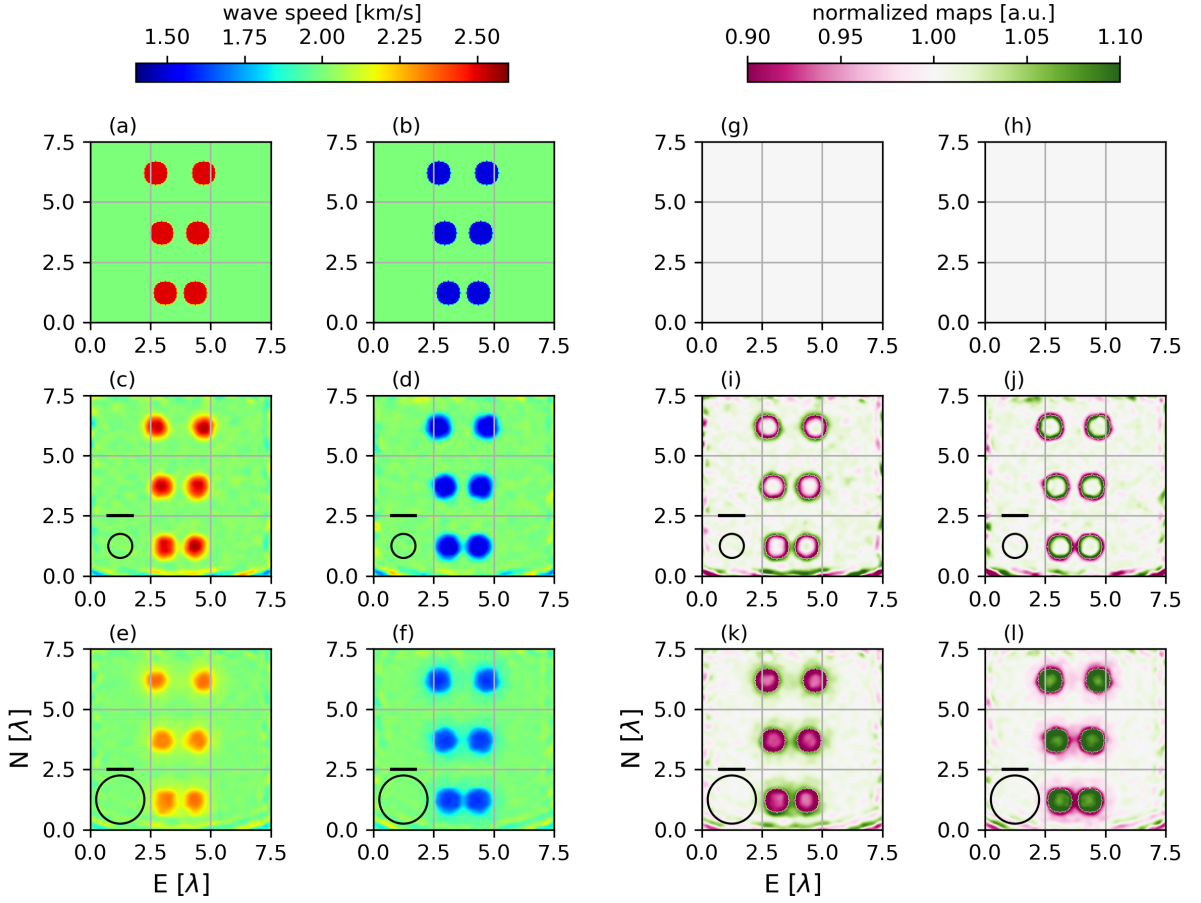


Figure 6. Results of the circular inclusion resolution test. The left two columns panels (a-f) show absolute values, the right two columns panels (g-l) show scaled values. (a-b) Input models of the three circular inclusion pairs separated by $1\lambda_0$, $0.5\lambda_0$, and $0.25\lambda_0$. The inclusion diameter is $1\lambda_0$. Focal spot images obtained with (c-d) $r_{\text{fit}} = 0.5\lambda_0$ and (e-f) $r_{\text{fit}} = 1\lambda_0$. (g-h) Normalized input wave speed map. (i-j) Images in (c-d) scaled by the corresponding input distributions in (a-b). (k-l) Images in (e-f) scaled by the corresponding input distributions in (a-b). In the lower two rows, the reference wavelength λ_0 is indicated by the black line and the r_{fit} range used for the nonlinear regression is the diameter of the black circle.

for both fitting ranges, and for the three different distances separating the inclusions. However, the contrast—the difference in ‘velocity amplitude’—depends on the fitting range. Using $r_{\text{fit}} = 1\lambda_0$ leads to larger errors on the velocity estimates. The quantitative aspect of the method decreases with an increase of the fitting range, which appears as an averaging effect, consistent with the observations across the interface in the half-space case. Panels in the right two columns in Figure 6 show the data from Figures 6(a-f) normalized by the input wave speed maps (Figs. 6a-b). The fact that circular features are visible in Figures 6(i-l) demonstrates that amplitudes are not accurately retrieved around the edges. The width of the halo or ΔL scales again with the fitting distance, the reconstruction benefits from smaller r_{fit} values (Figs. 6i-j).

These interpretations are supported by wave speed profiles across the inclusions (Fig. 7), which demonstrate again that the focal spot image quality, i.e., resolution and contrast, depends on the fitting range. Inclusions separated by $0.25\lambda_0$ (Figs. 7a-b) are well retrieved for small $r_{\text{fit}} = 0.5\lambda_0$. The wave speed value away from an

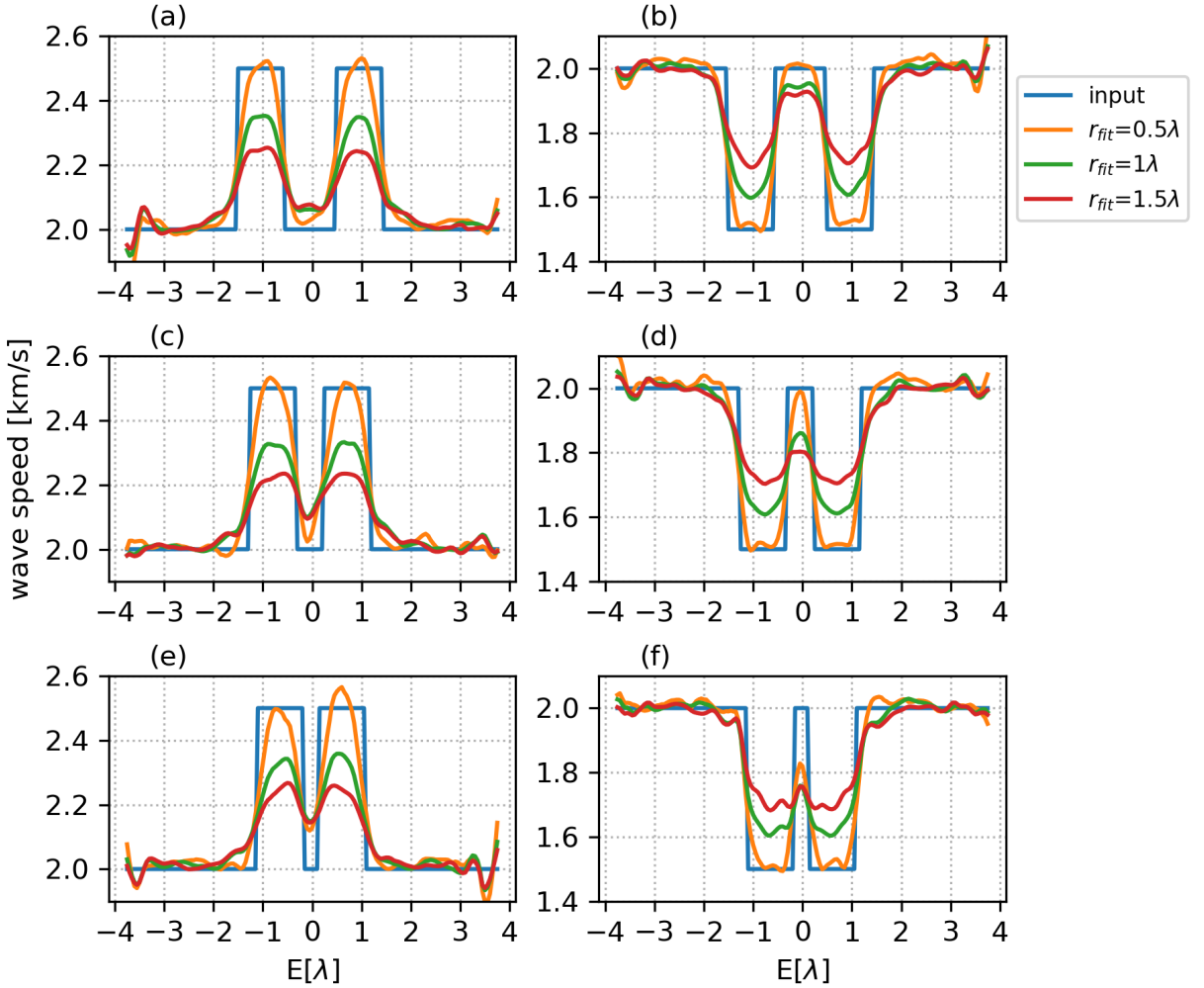


Figure 7. Cross sections through the circular inclusions. Profiles of input (blue) and estimated wave speeds for $r_{fit} = 0.5\lambda_0$ (orange), $r_{fit} = 1\lambda_0$ (green), and $r_{fit} = 1.5\lambda_0$ (red) for each pair of the circular inclusions. Results are obtained along the E-axis passing through the center of the inclusions. (a-b) Inclusions separated by $1\lambda_0$. (c-d) Inclusions separated by $0.5\lambda_0$. (e-f) Inclusions separated by $0.25\lambda_0$.

interface is well approximated. This applies to the stiff and the compliant inclusions. For $r_{fit} = 1\lambda_0$ the contrast cannot be recovered, which is linked to the fitting range dependent transition zone width that is here similar to the inclusion diameter. The same mechanism applies to the results obtained with $r_{fit} = 1.5\lambda_0$. Importantly, two inclusions can always be discriminated when the separation distance is $0.25\lambda_0$, which is yet more obvious from Figure 6. For a separation distance of $0.5\lambda_0$ this quality of the imaging approach increases, and inclusions are completely discriminated for a distance of $1\lambda_0$. Taken together, the fitting range dependent sensitivity of the resolution mostly affects the contrast estimate, but less so the ability to discriminate two objects. The power to discriminate inclusions separated by only $0.25\lambda_0$ suggests that the property of super-resolution applies, similar to focal spot medical imaging results obtained with ultrasound wavelengths [Zemzemi et al., 2020]. Focal spot imaging resolution thus benefits from high station density across short data ranges. The wave speed estimates are, however, sensitive to noisy near-field data. In turn, longer fitting distances reduce fluctuations, which leads

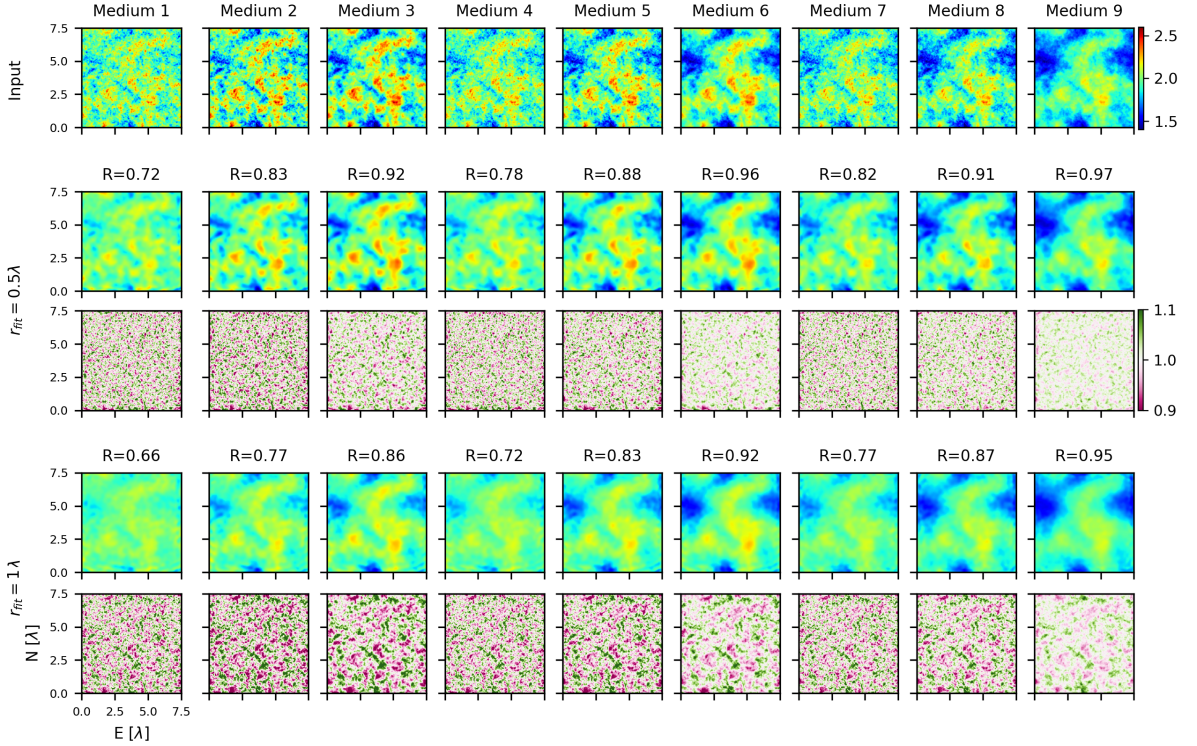


Figure 8. Results from the random media case. The top row shows the heterogeneous 2D velocity distributions that are synthesized using Equations 2 and 3. Values of the corresponding tuning parameters are given in Table 1. The center and bottom row show focal spot based images using $r_{\text{fit}} = 0.5\lambda_0$ and $r_{\text{fit}} = 1\lambda_0$.

to a trade-off between accuracy or contrast and resolution or discrimination [Giammarinaro et al., 2023].

3.4. Imaging random media

The last experiment explores focal spot imaging results of heterogeneous media that are characterized by a von Karman spectral density probability function (Eqs. 2, 3). Figure 8 shows input wave speed distributions and the images obtained with fitting ranges $r_{\text{fit}} = 0.5\lambda_0$ and $r_{\text{fit}} = 1\lambda_0$ together with the input-normalized images. For each case, we calculate a coefficient of correlation R between the input distribution and the image. As in the previous experimental configurations, the overall pattern of the velocity variations is well retrieved using focal spot imaging, i.e., there is no systematic phase bias. This is demonstrated by the fact that the R coefficient is maximum for the zero-lag auto-correlation. The smallest coefficient of correlation is $R = 0.66$ for Medium 1 ($a = 0.5\lambda_0$, $\kappa = 0.1$) and $r_{\text{fit}} = 1\lambda_0$, which corresponds to small scale, high contrast wave speed variations and the longer fitting range. The best estimation is obtained for Medium 9 ($a = 2\lambda_0$, $\kappa = 0.6$) imaged with $r_{\text{fit}} = 0.5\lambda_0$, which corresponds to analysis using shorter ranges than the correlation length a . This leads to a high coefficient of correlation $R = 0.97$. Increasing r_{fit} to $1\lambda_0$ yields $R = 0.95$. We can again confirm previous results, the images become smoother with increasing r_{fit} , which is synonymous with a loss in contrast and hence details. The other way around, the smoother the input distribution for larger a and κ (Medium 3, 6, 9), the better is the estimate. The corresponding normalized results illustrate the imaging quality in a complementary style. Predominantly gray distributions indicate good reconstructions, the red-green pattern value range correlates

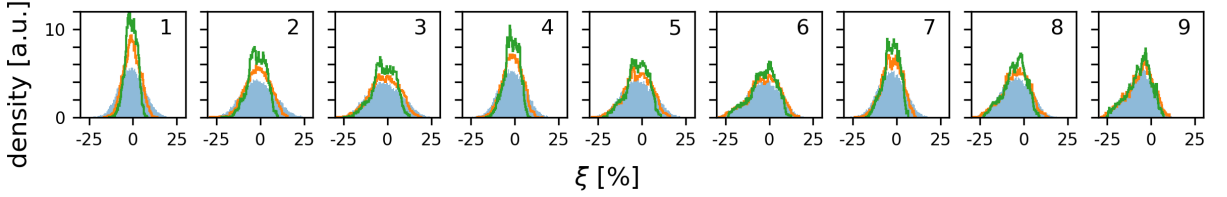


Figure 9. Histograms of the relative wave speed change ξ for the nine media imaged in Figure 8. Blue data correspond to the input reference values, and orange and green data correspond to images obtained with $r_{\text{fit}} = 0.5\lambda_0$ and $r_{\text{fit}} = 1\lambda_0$.

with the amplitude mismatch, and the color-speckle size is related to r_{fit} . The green ‘channel’ feature around position (3,2.5) illustrates a narrow low-velocity zone that is overestimated by the averaging, longer $r_{\text{fit}} = 1\lambda_0$.

We estimate the relative wave speed change ξ from the wave speed images by inverting Equation 1

$$\xi(\mathbf{x}) = V/V_0 - 1, \quad (4)$$

with $V_0 = 2$ km/s. We compile histograms of the ξ distributions to compare properties of the reference input distributions and of the images. Figure 9 collects the ξ histograms from the input and from the estimates for $r_{\text{fit}} = 0.5\lambda_0$ and $r_{\text{fit}} = 1\lambda_0$. The similarity between reference and image is better for $r_{\text{fit}} = 0.5\lambda_0$ than $r_{\text{fit}} = 1\lambda_0$. The best result is obtained for Medium 9 which shows very similar histograms. The histograms obtained with $r_{\text{fit}} = 1\lambda_0$ are more narrow and have a higher peak value around small ξ values compared to the $r_{\text{fit}} = 0.5\lambda_0$ results. This indicates again the low-pass filter property of larger fitting ranges observed in the previous experiments.

4. Discussion

Resolution can mean different things in different imaging contexts, including the number or density of measuring points, the spectral sensitivity of an imaging device or method, the ability to detect or discriminate features and to accurately estimate their properties, contrast in brightness or color, or phase fidelity [Smith, 2013]. We use numerical simulations of two-dimensional acoustic wave propagation in a cavity (Figs. 1, 2) to investigate the lateral resolution of the focal spot imaging technique for a fixed acquisition system with a constant number of grid points. The increase in depth resolution for such a compact dense array configuration compared to measurements made on traveling waves is established by Giammarinaro et al. [2023]. We implement four test cases that together allow us to deduce the resolution power of seismic Rayleigh wave focal spots reconstructed from vertical-vertical component noise correlation data. Lateral resolution is discussed as the ability to resolve a step function in the material properties, to discriminate and characterize two closely spaced objects, and to measure position, amplitude, and phase of so-called random distributions.

In a first homogeneous control experiment (Figs. 2, 3) the reference wave speed is estimated with an error below 2% on average, which includes, however, areas of larger error affected by edge effects. This error is larger compared to the focal spot results based on numerical time-reversal experiments, where noise-free synthetics lead to errors in the 0.01% range for vertical-vertical component data and fitting distances of $r_{\text{fit}} = 0.5\lambda_0$ and $r_{\text{fit}} = 1\lambda_0$, and where anisotropic surface wave incidence results in biases in the 0.1% range [Giammarinaro et al., 2023]. The different error levels are associated with the different methods used to synthesize Green’s functions and focal spots. In time-reversal experiments, the wave field and hence the ballistic wave correlations are fully controlled by the mirror properties. More mirror elements lead to better refocusing results. Controlled lab experiments can stack over different space realizations. In seismic data applications an improved Green’s function and refocusing reconstruction is achieved by time averaging to better conform with the decorrelated noise source assumption. Here, the focal spots are retrieved from cross-correlation of the reverberating cavity

wave field, where the quality of the Green's function is controlled by the ability to excite and average a sufficiently large number of modes in the cavity [Draeger and Fink, 1999]. Hence we stack over different realizations using different source positions to increase the number of independent modes to enhance the narrow-band refocusing, which is equivalent to using more time reversal mirror elements in a time-reversal experiment. Our approach converges towards the theoretical focal spot, but it remains sensitive to details of the implementation such as the source positions of the relatively few realizations. This means that the imperfect cavity results are comparable to focal spots obtained from noisy data.

The second half-spaces experiment (Figs. 4, 5) shows the feasibility to resolve the contrast between two media that have a 10 % difference in wave speed. However, the interface is not perfectly resolved. Whereas the wave speed is correctly estimated away from the interface, the finite fitting range creates an averaging or low-pass filter effect that depends on r_{fit} . Tests with different r_{fit} values indicate that the transition width ΔL scales with a good approximation linearly with the fitting range, $\Delta L \approx r_{\text{fit}}$.

The third circular inclusion configuration (Figs. 6, 7) shows that it is possible to discriminate two separate objects distanced by $0.25\lambda_0$, even for fitting ranges of one wavelength. However, the low-pass filter properties lead to averaged amplitude values, which therefore depends on the fitting range. We have not observed situations where the focal spot method yields biased phase properties, so the inclusion positions are accurate. This suggests that the super-resolution property demonstrated with passive elastography in soft tissues [Zemzemi et al., 2020] also applies to 2D Rayleigh surface wave propagation. Again this means that for good data quality and high station density the method has the potential to meet the formal criterion of super-resolution, i.e., the sensitivity at small scales is sufficient to discriminate objects or features that are separated by distances that are much shorter than the wavelength.

The fourth test case considers random media (Figs. 8, 9, Table 1) which show the highest similarity to distributions of Earth material properties. The quality of the focal spot reconstruction as quantified by the correlation coefficient R between reference and image depends on the roughness or smoothness of the distribution in relation to wavelength and fitting distance. R is small when the distributions are rough, have small-scale fluctuations compared to the probing wavelength, and the fitting distance is large. The reconstruction is almost perfect when the distributions are smooth, have large-scale fluctuations, and the fitting distance is small. These conclusions are further corroborated comparing histogram properties of the velocity variation parameter ξ (Eq. 2, Fig. 9), which again demonstrate the low-pass filtering effect of large r_{fit} values. Thus, positions are well estimated but the amplitudes diverge for small-scale heterogeneities. The best estimates are obtained for variations on scales larger than r_{fit} . If resources permit, an imaging campaign could be optimized by first detecting target features with low contrast before then a sensor re-configuration helps to improve the quantitative estimate by increasing the signal-to-noise ratio through network densification.

The present study employs two-dimensional acoustic simulations. They present the advantage of being scalar simulations yielding the same Green's function as for vertical-vertical component Rayleigh wave propagation. Our main conclusions thus hold for seismic Rayleigh wave imaging. However, this set-up does not allow to study the biasing effect of interfering body wave energy. Giammarinaro et al. [2023] showed that the error on the vertical-vertical component increases in the presence of P body waves, but this can be compensated for by increasing the fitting range. Together with our observations here this implies that an increase in r_{fit} improves the results if refocusing P wave energy distorts the surface wave focal spot, but that this remedy has an adverse impact on the lateral resolution power. This trade-off situation would benefit from efficient spatial noise auto-correlation or focal spot filters. Alternatively, Rayleigh wave phase speed estimates obtained from radial-vertical component data are much less sensitive to P -waves [Giammarinaro et al., 2023], which offers independent constraints for the improvement of vertical-vertical results.

5. Conclusion

We investigate the lateral resolution power of the surface wave focal spot imaging method using numerical experiments of reverberating wave fields in a cavity. Most importantly the resolution depends on the fitting

range. This means that focal spot imaging exhibits super-resolution properties provided the data quality supports sub-wavelength fitting ranges. Longer fitting ranges still allow imaging of small-scale features at super-resolution albeit with a loss in contrast. In conclusion, seismic surface wave focal spot imaging shows convincing resolution properties that make it suitable for a wide range of imaging applications ranging from feature detection to accurate wave speed estimates. There are hence no fundamental disadvantages compared to established passive surface wave tomography methods. Here as there, the station configuration can be tuned to support image quality and properties for different goals. Here as there, data quality or signal-to-noise ratio ultimately has the largest impact on the resolution, i.e., on the ability to discriminate features, and to accurately estimate their properties.

Conflicts of interest

The authors declare no competing financial interest.

Open research / data availability

Dedication

The manuscript was written with contributions from all authors. All authors have given approval to the final version of the manuscript.

Acknowledgments

We thank Julien de Rosny, Stefan Catheline, Michel Campillo, Léonard Seydoux, Alexander Meaney, and Markus Juvonen for helpful discussions. This work was sponsored by a research grant from the Academy of Finland (decision number 322421). We thank Editor N.N., and reviewers N.N. and N.N. for comments that helped to improve the manuscript.

References

- Aki, K. (1957). Space and time spectra of stationary stochastic waves, with special reference to microtremors. *Bulletin of the Earthquake Research Institute*, 35, 415–456.
- Asten, M. W. (2006). On bias and noise in passive seismic data from finite circular array data processed using SPAC methods. *Geophysics*, 71(6), V153–V162.
- Barrere, V., Melodelima, D., Catheline, S., and Giammarinaro, B. (2020). Imaging of thermal effects during high-intensity ultrasound treatment in liver by passive elastography: A preliminary feasibility in vitro study. *Ultrasound Med. Biol.*, 46, 1968–1977. <https://linkinghub.elsevier.com/retrieve/pii/S0301562920301356>.
- Ben-Zion, Y. (1989). The response of two joined quarter spaces to *SH* line sources located at the material discontinuity interface. *Geophys. J. Int.*, 98(2), 213–222. <https://academic.oup.com/gji/article-lookup/doi/10.1111/j.1365-246X.1989.tb03346.x>.
- Benech, N., Brum, J., Catheline, S., Gallot, T., and Negreira, C. (2013). Near-field effects in green's function retrieval from cross-correlation of elastic fields: experimental study with application to elastography. *J. Acoust. Soc. Am.*, 133, 2755–66. <http://www.ncbi.nlm.nih.gov/pubmed/23654383><http://asa.scitation.org/doi/10.1121/1.4795771>.
- Brum, J., Catheline, S., Benech, N., and Negreira, C. (2015). Quantitative shear elasticity imaging from a complex elastic wavefield in soft solids with application to passive elastography. *IEEE Trans. Ultrason. Ferroelectr. Freq. Control*, 62(4), 673–685. <http://ieeexplore.ieee.org/document/7081463/>.
- Catheline, S., Benech, N., Brum, J., and Negreira, C. (2008). Time Reversal of Elastic Waves in Soft Solids. *Phys. Rev. Lett.*, 100(6), 064301. <https://link.aps.org/doi/10.1103/PhysRevLett.100.064301>.

- Catheline, S., Souchon, R., Rupin, M., Brum, J., Dinh, A. H., and Chapelon, J.-Y. (2013). Tomography from diffuse waves: Passive shear wave imaging using low frame rate scanners. *Appl. Phys. Lett.*, 103(1), 014101.
- Chamarczuk, M., Malinowski, M., Nishitsuji, Y., Thorbecke, J., Koivisto, E., Heinonen, S., Juurela, S., Mężyk, M., and Draganov, D. (2019). Automatic 3D illumination-diagnosis method for large- N arrays: Robust data scanner and machine-learning feature provider. *Geophysics*, 84(3), Q13–Q25. <https://library.seg.org/doi/10.1190/geo2018-0504.1>.
- Cotton, F. and Coutant, O. (1997). Dynamic stress variations due to shear faults in a plane-layered medium. *Geophys. J. Int.*, 128, 676–688.
- Cox, H. (1973). Spatial correlation in arbitrary noise fields with application to ambient sea noise. *J. Acoust. Soc. Am.*, 54, 1289–1301.
- Derode, A., Larose, E., Tanter, M., de Rosny, J., Tourin, A., Campillo, M., and Fink, M. (2003). Recovering the Green's function from field-field correlations in an open scattering medium (L). *J. Acoust. Soc. Am.*, 113(6), 2973.
- Draeger, C. and Fink, M. (1999). One-channel time-reversal in chaotic cavities: Theoretical limits. *J. Acoust. Soc. Am.*, 105(2), 611–617. <http://asa.scitation.org/doi/10.1121/1.426251>.
- Ekström, G. (2014). Love and Rayleigh phase-velocity maps, 5–40 s, of the western and central USA from USArray data. *Earth Planet. Sci. Lett.*, 402(C), 42–49.
- Ekström, G., Abers, G. A., and Webb, S. C. (2009). Determination of surface-wave phase velocities across USArray from noise and Aki's spectral formulation. *Geophys. Res. Lett.*, 36(18), 5–9.
- Fink, M. (1997). Time reversed acoustics. *Physics Today*, 50(3), 34–40.
- Frankel, A. and Clayton, R. W. (1986). Finite difference simulations of seismic scattering: Implications for the propagation of short-period seismic waves in the crust and models of crustal heterogeneity. *J. Geophys. Res.*, 91(B6), 6465. <http://doi.wiley.com/10.1029/JB091iB06p06465>.
- Gallot, T., Catheline, S., Roux, P., Brum, J., Benech, N., and Negreira, C. (2011). Passive elastography: shear-wave tomography from physiological-noise correlation in soft tissues. *IEEE Trans. Ultrason. Ferroelectr. Freq. Control*, 58(6), 1122–1126. <http://ieeexplore.ieee.org/document/5895024/https://ieeexplore.ieee.org/document/5895024/>.
- Giammarinaro, B. and Hillers, G. (2022). Resources for "seismic surface wave focal spot imaging: numerical resolution experiments". University of Helsinki.
- Giammarinaro, B., Tsarsitalidou, C., Hillers, G., de Rosny, J., Seydoux, L., Catheline, S., Campillo, M., and Roux, P. (2023). Seismic surface wave focal spot imaging: numerical resolution experiments. *Geophys. J. Int.* <https://academic.oup.com/gji/advance-article/doi/10.1093/gji/ggac247/6618556>.
- Haney, M. M., Mikesell, T. D., van Wijk, K., and Nakahara, H. (2012). Extension of the spatial autocorrelation (SPAC) method to mixed-component correlations of surface waves. *Geophys. J. Int.*, 191(1), 189–206.
- Haney, M. M. and Nakahara, H. (2014). Surface-wave Green's tensors in the near field. *Bull. Seism. Soc. Am.*, 104(3), 1578–1586.
- Hillers, G., Mai, P. M., Ben-Zion, Y., and Ampuero, J.-P. (2007). Statistical properties of seismicity of fault zones at different evolutionary stages. *Geophys. J. Int.*, 169, 515–533.
- Hillers, G., Roux, P., Campillo, M., and Ben-Zion, Y. (2016). Focal spot imaging based on zero lag cross-correlation amplitude fields: Application to dense array data at the San Jacinto fault zone. *J. Geophys. Res. Solid Earth*, 121(11), 8048–8067.
- Holliger, K. and Levander, A. R. (1992). A stochastic view of lower crustal fabric based on evidence from the Ivrea Zone. *Geophys. Res. Lett.*, 19(11), 1153–1156. <http://doi.wiley.com/10.1029/92GL00919>.
- Lin, F.-C. and Ritzwoller, M. H. (2011). Helmholtz surface wave tomography for isotropic and azimuthally anisotropic structure. *Geophysical Journal International*, 186(3), 1104–1120. <https://doi.org/10.1111/j.1365-246X.2011.05070.x>, <https://arxiv.org/abs/https://academic.oup.com/gji/article-pdf/186/3/1104/5929969/186-3-1104.pdf>.
- Lin, F.-C., Ritzwoller, M. H., and Snieder, R. (2009). Eikonal tomography: surface wave tomography by phase front tracking across a regional broad-band seismic array. *Geophys. J. Int.*, 177(3), 1091–1110. <https://doi.org/10.1111/j.1365-246X.2009.04281.x>.

- [//academic.oup.com/gji/article-lookup/doi/10.1111/j.1365-246X.2009.04105.x](http://academic.oup.com/gji/article-lookup/doi/10.1111/j.1365-246X.2009.04105.x).
- Liu, Q. and Gu, Y. (2012). Seismic imaging: From classical to adjoint tomography. *Tectonophysics*, 566-567, 31–66.
- Mai, P. M. and Beroza, G. C. (2002). A spatial random field model to characterize complexity in earthquake slip: RANDOM FIELD MODEL FOR EARTHQUAKE SLIP. *J. Geophys. Res. Solid Earth*, 107(B11), ESE 10–1–ESE 10–21. <http://doi.wiley.com/10.1029/2001JB000588>.
- Obermann, A., Planès, T., Hadziioannou, C., and Campillo, M. (2016). Lapse-time-dependent coda-wave depth sensitivity to local velocity perturbations in 3-D heterogeneous elastic media. *Geophys. J. Int.*, 207(1), 59–66. <https://academic.oup.com/gji/article-lookup/doi/10.1093/gji/ggw264>.
- Ripperger, J., Ampuero, J.-P., Mai, P. M., and Giardini, D. (2007). Earthquake source characteristics from dynamic rupture with constrained stochastic fault stress: DYNAMIC RUPTURE WITH STOCHASTIC FAULT STRESS. *J. Geophys. Res. Solid Earth*, 112(B4). <http://doi.wiley.com/10.1029/2006JB004515>.
- Sabra, K. G., Conti, S., Roux, P., and Kuperman, W. A. (2007). Passive in vivo elastography from skeletal muscle noise. *Appl. Phys. Lett.*, 90(19), 194101. <http://aip.scitation.org/doi/10.1063/1.2737358>.
- Sabra, K. G., Gerstoft, P., Roux, P., Kuperman, W. A., and Fehler, M. C. (2005). Surface wave tomography from microseisms in Southern California. *Geophys. Res. Lett.*, 32(14), 1–4.
- Sanchez-Sesma, F. J. (2006). Retrieval of the Green's Function from Cross Correlation: The Canonical Elastic Problem. *Bull. Seism. Soc. Am.*, 96(3), 1182–1191.
- Sato, H., Fehler, M. C., and Maeda, T. (2012). *Seismic Wave Propagation and Scattering in the Heterogeneous Earth: Second Edition*. SpringerLink. Springer Berlin Heidelberg, 2nd ed edition.
- Shapiro, N. M. and Campillo, M. (2004). Emergence of broadband Rayleigh waves from correlations of the seismic ambient noise. *Geophys. Res. Lett.*, 31, article no. L07614.
- Smith, S. (2013). *Digital signal processing: a practical guide for engineers and scientists*. Elsevier.
- Treeby, B. E., Budisky, J., Wise, E. S., Jaros, J., and Cox, B. T. (2018). Rapid calculation of acoustic fields from arbitrary continuous-wave sources. *J. Acoust. Soc. Am.*, 143(1), 529–537.
- Tromp, J., Tape, C., and Liu, Q. (2005). Seismic tomography, adjoint methods, time reversal and banana-doughnut kernels. *Geophys. J. Int.*, 160(1), 195–216.
- Tsai, V. C. and Moschetti, M. P. (2010). An explicit relationship between time-domain noise correlation and spatial autocorrelation (SPAC) results. *Geophys. J. Int.*, 182(1), 454–460.
- Tsarsitalidou, C., Boué, P., Hillers, G., Giammarinaro, B., Campillo, M., Seydoux, L., and Stehly, L. (2021). Seismic imaging with focusing surface waves obtained from USArray noise correlation functions. <https://meetingorganizer.copernicus.org/EGU21/EGU21-9045.html>.
- Weertman, J. (1980). Unstable slippage across a fault that separates elastic media of different elastic constants. *J. Geophys. Res. Solid Earth*, 85(B3), 1455–1461. <http://doi.wiley.com/10.1029/JB085iB03p01455>.
- Yokoi, T. and Margaryan, S. (2008). Consistency of the spatial autocorrelation method with seismic interferometry and its consequence. *Geophysical Prospecting*, 56, 435–451.
- Zemzemi, C., Zorgani, A., Daunizeau, L., Belabhar, S., Souchon, R., and Catheline, S. (2020). Super-resolution limit of shear-wave elastography. *Europhys. Lett.*, 129(3), 34002.
- Zorgani, A., Souchon, R., Dinh, A.-H., Chapelon, J.-Y., Ménager, J.-M., Lounis, S., Rouvière, O., and Catheline, S. (2015). Brain palpation from physiological vibrations using mri. *Proc. Natl. Acad. Sci. USA*, 112, 12917–12921.